How to cite: *Angew. Chem. Int. Ed.* **2024**, *63*, e202319239
doi.org/10.1002/anie.202319239

Electrocatalytic H_2O Splitting

Cobalt-based Co_3Mo_3N/Co_4N/Co Metallic Heterostructure as a Highly Active Electrocatalyst for Alkaline Overall Water Splitting

Yuanwu Liu[+], Lirong Wang[+], René Hübner, Johannes Kresse, Xiaoming Zhang, Marielle Deconinick, Yana Vaynzof, Inez M. Weidinger, and Alexander Eychmüller**

Abstract: Alkaline water electrolysis holds promise for large-scale hydrogen production, yet it encounters challenges like high voltage and limited stability at higher current densities, primarily due to inefficient electron transport kinetics. Herein, a novel cobalt-based metallic heterostructure (Co_3Mo_3N/Co_4N/Co) is designed for excellent water electrolysis. In operando Raman experiments reveal that the formation of the Co_3Mo_3N/Co_4N heterointerface boosts the free water adsorption and dissociation, increasing the available protons for subsequent hydrogen production. Furthermore, the altered electronic structure of the Co_3Mo_3N/Co_4N heterointerface optimizes ΔG_H of the nitrogen atoms at the interface. This synergistic effect between interfacial nitrogen atoms and metal phase cobalt creates highly efficient active sites for the hydrogen evolution reaction (HER), thereby enhancing the overall HER performance. Additionally, the heterostructure exhibits a rapid OH^- adsorption rate, coupled with great adsorption strength, leading to improved oxygen evolution reaction (OER) performance. Crucially, the metallic heterojunction accelerates electron transport, expediting the afore-mentioned reaction steps and enhancing water splitting efficiency. The Co_3Mo_3N/Co_4N/Co electrocatalyst in the water electrolyzer delivers excellent performance, with a low 1.58 V cell voltage at 10 mA cm^{-2}, and maintains 100 % retention over 100 hours at 200 mA cm^{-2}, surpassing the Pt/C||RuO_2 electrolyzer.

1. Introduction

Water electrolysis is a promising technology to address the global energy crisis by providing a green and scalable strategy to convert electricity from renewable energy sources into hydrogen fuel. Compared to acidic electrolyzers, the alkaline electrolyzers are more popular in the industry due to their cheaper ion exchange membranes and faster oxygen evolution reaction (OER) kinetics.[1,2] However, this brings forth a new disadvantage: the hydrogen evolution reaction (HER) kinetics is two orders of magnitude slower when using an alkaline electrolyte than when using an acidic electrolyte.[3] Based on earlier work, the bottleneck of alkaline water electrolysis, especially alkaline HER, is largely related to the sluggish water dissociation step (Volmer and Heyrovsky steps).[4] In the Volmer step, the HO–H bond is broken as it interacts with an electron, ultimately forming an adsorbed hydrogen atom (H_{ad}). In the Heyrovsky step, H_{ad} will combine with another broken HO–H bond and an electron to form H_2. To date, noble-metal-based catalysts (NMC) are still regarded as the state-of-the-art electrocatalysts due to their high conductivity, strong water dissociation ability, and optimal *d*-band center for adsorbing H^+/OH^-.[5,6] NMC, however, are expensive and unstable in long-term reaction processes, limiting their large-scale application.[7] From the perspective of commercialization, it is urgent to develop non-noble metal catalysts with high catalytic activity and good durability.

In general, an ideal bifunctional non-noble-metal alkaline electrocatalyst should satisfy the following conditions: 1) a sufficient number of active sites for fast adsorption of H_2O/OH^- and strong H_2O dissociation ability; 2) the

[*] Y. Liu,[+] J. Kresse, Prof. A. Eychmüller
Physical Chemistry, TU Dresden, Zellescher Weg 19, 01069 Dresden, Germany
E-mail: alexander.eychmueller@tu-dresden.de

L. Wang,[+] Prof. X. Zhang
School of Materials Science and Engineering, Hebei University of Technology, Tianjin 300130, China
E-mail: zhangxiaoming87@hebut.edu.cn

Dr. R. Hübner
Institute of Ion Beam Physics and Materials Research, Helmholtz-Zentrum Dresden-Rossendorf e.V., Bautzner Landstrasse 400, 01328 Dresden, Germany

M. Deconinick, Prof. Y. Vaynzof
Chair for Emerging Electronic Technologies, TU Dresden, Nöthnitzer Str. 61, Dresden, 01187 Sachsen, Germany
and
Leibniz-Institute for Solid State and Materials Research Dresden, Helmholtzstraße 20, Dresden, 01069 Sachsen, Germany

Prof. I. M. Weidinger
Fakultät Chemie und Lebensmittelchemie, Technische Universität Dresden, Zellescher Weg 19, 01069 Dresden, Germany

[+] Y. Liu and L. Wang contributed equally to this work.

adsorption of H at the active sites is neither too strong nor too weak, i.e., the Gibbs free energy for H_{ad} (ΔG_H) is close to zero;[8] 3) high conductivity that enables rapid electron transport from the interior of the catalyst to the catalytic reaction interface; 4) good mechanical stability and catalytic durability. Recently, cobalt-based compounds, especially a class of interstitial compounds with noble metal properties (cobalt nitrides), have exhibited great potential for alkaline water splitting. Metallic Co_4N, a typical member of the cobalt nitride family, has been reported to have better OER performance than benchmark IrO_2 because the Co atom in Co_4N is prone to adsorb OH^-.[9,10] Nevertheless, the Co atoms in Co_4N have a strong adsorption of H and require high energy to dissociate water, resulting in poor HER activity. Introducing metallic Co as HER sites is an effective method to optimize ΔG_H, because Co has a more suitable ability to adsorb and desorb hydrogen.[11,12] Additionally, coupling Co_4N with a secondary phase, such as CeO_2,[9] CoO,[13] Co_2P,[14] or NiFe double-layer hydroxides[15] is widely used to modify the water dissociation energy. However, the majority of secondary phase reported to couple with Co_4N are semiconductor-based, which result in a suppressed electron transport efficiency in electrocatalysts. To create high-performance electrocatalysts for alkaline water electrolysis, it is vital to continue developing Co_4N-based metallic heterostructures with good electrical conductivity.

The incorporation of molybdenum atoms into Co_4N can result in the formation of an alternative metal phase known as Co_3Mo_3N.[16,17] Unlike pure Co_4N, Co_3Mo_3N exhibits an enhanced d-state density near the Fermi level. Additionally, the introduction of molybdenum atoms into Co_4N prompts electron transfer from Mo to Co atoms. This electron transfer optimizes the capacity of Co atoms to efficiently adsorb and desorb H atoms. Consequently, the unique electronic structure of Co_3Mo_3N establishes it as a superb electrocatalyst for HER. The synergy of Co_3Mo_3N and Co_4N may ensure effective electron transfer, simultaneously addressing the challenge of insufficient HER activity observed in pure Co_4N. Consequently, Co_3Mo_3N emerges as an ideal material for constructing Co_4N-based metallic heterostructures.

In this work, we design a new bifunctional electrocatalyst made of $Co_3Mo_3N/Co_4N/Co$ composite material with metallic properties, which perfectly meets the above requirements for alkaline water electrolysis. The formation of the Co_3Mo_3N/Co_4N interface plays a crucial role in enhancing the water adsorption capacity and significantly reducing the energy barrier for water dissociation. Additionally, the interface optimization influences the electronic structure of the N atoms, reducing ΔG_H close to 0, and the introduction of metallic cobalt further optimizes ΔG_H of the electrocatalyst. As a result, the $Co_3Mo_3N/Co_4N/Co$ heterostructure demonstrates outstanding performance in the HER. Moreover, the upshift of the transition metal *d*-band center contributes to an increased adsorption capacity of the cobalt sites in the electrocatalyst, particularly for OH^-, favoring the OER. Furthermore, the metallic conductivity in $Co_3Mo_3N/Co_4N/Co$ facilitates efficient electron transfer and transport within the catalyst and at the catalyst/electrolyte interface. By integrating the afore-mentioned improvements, $Co_3Mo_3N/Co_4N/Co$ shows remarkable performances with low overpotentials of 220 mV for the OER and 78 mV for the HER in a 1 M KOH electrolyte at 10 mA cm^{-2}. Moreover, the water electrolyzer operates efficiently with an exceptionally low cell voltage of only 1.58 V at 10 mA cm^{-2} and exhibits outstanding durability even under demanding conditions of 200 mA cm^{-2}. In this work, innovative perspectives on improving the overall water splitting performance of transition-metal-based metallic heterostructures are presented, with a focus on improving their stability under high current densities.

2. Results and discussion

The synthesis of the metallic $Co_3Mo_3N/Co_4N/Co$ heterostructure involves two principal stages, the ion exchange of molybdate ions (MoO_4^{2-}) with the Zeolitic Imidazolate Framework-L (ZIF–L) and the pyrolytic process of the precursor (as shown in Figure 1). Specifically, it starts with synthesizing ZIF–L wires on the surface of carbon cloth using a solvent method at room temperature. As shown in Figure 2a and Figure S1, high-density ZIF–L nanowires are distributed uniformly on the surface of the carbon cloth fibers. Subsequently, a fraction of the cobalt sites in ZIF–L are replaced by MoO_4^{2-} to produce the Mo/ZIF–L structure through ion exchange. Specifically, in the weak base solutions, the 2-MI ligand in ZIF–L will bind to H^+ (due to reversible hydrolysis of H_2O), triggering the diffusion of a small amount of Co^{2+} outwards.[18,19] Afterwards, some cobalt vacancies are formed, and MoO_4^{2-} will enter the cobalt vacancy and bond with unsaturated cobalt ions in the neighboring sites.[20] During this process, the morphology of Mo/ZIF–L is almost identical to that of ZIF–L, except that the diameter of the nanowires decreases (Figure S2a and S2b). This is due to the partial hydrolysis of the ZIF–L surface during the long-term ion exchange process, which is also proved by the TEM analysis (Figure S3). The shift of the XRD peaks to smaller angles signifies that some of the interplanar distances in ZIF–L have increased, indicating the successful incorporation of MoO_4^{2-} into the lattice (as demonstrated in Figure S2c and S2d). Finally, at high temperature, the released N atoms from the 2-methylimidazole react with Mo and Co atoms to form Co_3Mo_3N and Co_4N and the C-skeleton of the organic ligands forms a carbon framework. In addition, some cobalt ions are reduced to metallic cobalt by carbon at high temperature. In Figure 2b and Figure S4, after high-temperature pyrolysis, the wires basically maintain their morphology, and it is reported that this wire array can prevent gas bubbles from accumulating on the catalyst surface, which facilitates mass diffusion.[21] Further, the crystallinity and phase purity of the pre-fabricated products are measured by XRD. In Figure 2c, all the samples show a peak at 26°, which can be attributed to the (002) plane of graphitic carbon (PDF#75-0444).[22] In Figure S5, for Co_4N/Co, the diffraction maxima at 35.5°, 44°, 52°, and 76° match well with the cubic phase of Co_4N with

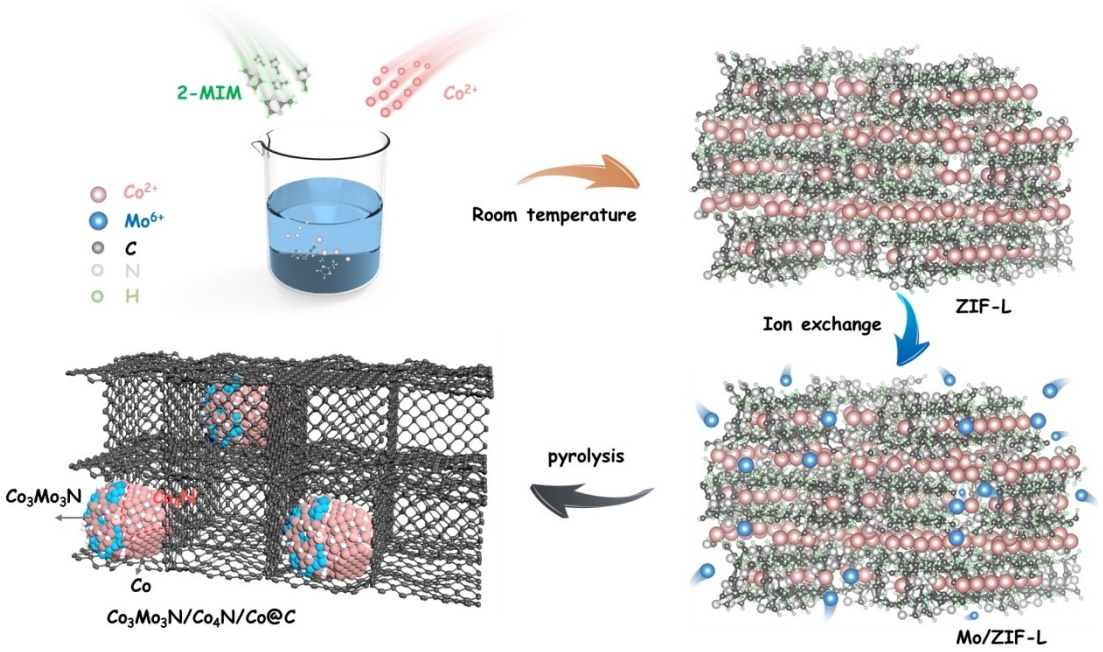

Figure 1. Schematic illustration of the synthetic process of $Co_3Mo_3N/Co_4N/Co$.

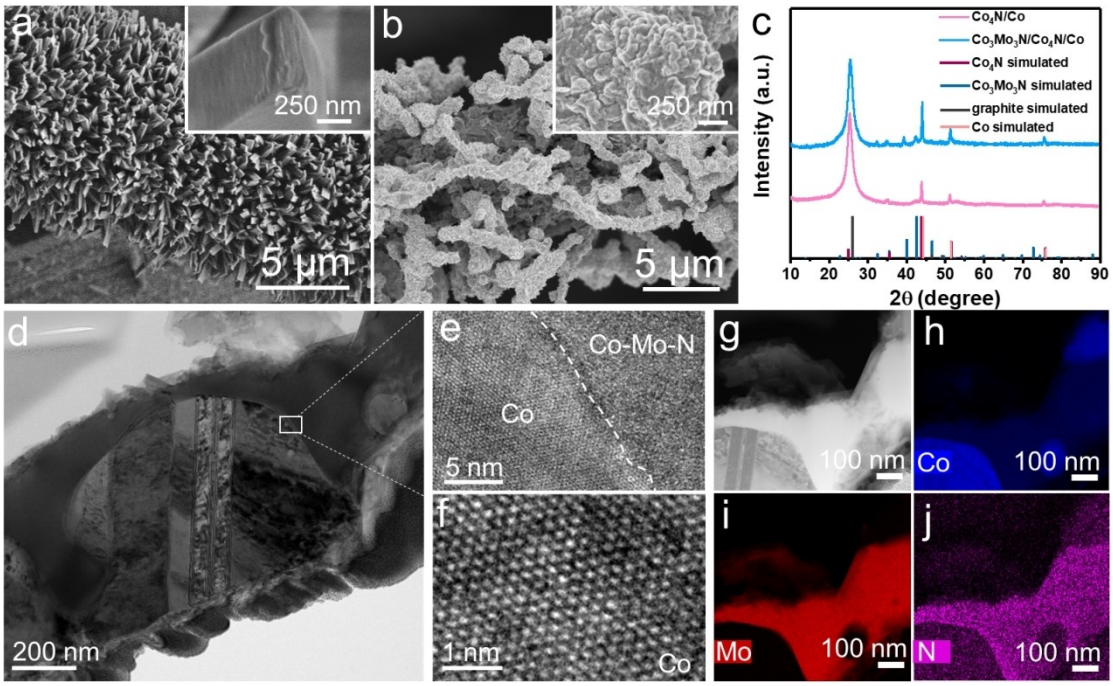

Figure 2. SEM image of (a) ZIF–L and (b) $Co_3Mo_3N/Co_4N/Co$ on carbon cloth. (c) XRD patterns of $Co_3Mo_3N/Co_4N/Co$ and Co_4N/Co. (d) Cross-sectional bright-field TEM image of a $Co_3Mo_3N/Co_4N/Co$ wire; (e) interface region between Co and Co–Mo–N as indicated in the panel (d). (f) high-resolution TEM image of the Co region. (g–j) HAADF-STEM image (g) and corresponding element distribution maps for Co (h), Mo (i), and N (j). The insets in panels (a) and (b) are high-magnification SEM images of ZIF–L and $Co_3Mo_3N/Co_4N/Co$, respectively.

the space group *Pm3 m* (ICDD 04–021-6262),[10] indicating its presence in the sample. However, the peaks at 44°, 52° and 76° are slightly shifted compared to Co_4N and are between the main peaks of cubic cobalt and Co_4N, indicating that Co_4N and Co can be present at the same time. For $Co_3Mo_3N/Co_4N/Co$, except for the graphitic carbon, Co, and Co_4N phases, all of the characteristic peaks are well compatible with the *FCC* Co_3Mo_3N phase with the space group *Fd3 m* (PDF#89-7953).[23] Furthermore, no other obvious peaks were detected, demonstrating that the nano-

composites are composed of Co_3Mo_3N, Co_4N, Co, and graphite. Raman results also confirm the presence of graphite, Co_4N, and Co_3Mo_3N (Figure S6). In addition, Co_3Mo_3N/Co_4N/Co at different pyrolytic temperatures were also characterized by SEM, XRD and Raman spectroscopy (Figure S7 and Figure S8).

To further reveal detailed information about the interfaces in the metallic Co_3Mo_3N/Co_4N/Co heterostructure, cross-sectional transmission electron microscopy (TEM) was conducted. In Figure 2d, the bright-field TEM image of a single wire, as they are visible in the SEM image of Figure 2b, clearly shows several interfaces. One of them is enlarged in the high-resolution image of Figure 2e. Element distribution analysis based on energy-dispersive X-ray spectroscopy (EDXS) indicates interfacing Co and Co–Mo–N regions (Figure 2g–2j). It should be mentioned that the N signal in the crystalline Co region (Figure 2f) is at the noise level, so a potential N content is below the detection limit of about 0.1 at.%.

The composition of the synthesized samples was analyzed by X-ray photoelectron spectroscopy (XPS). In Figure S9a, a clear contribution of the Mo 3d peak is observed in the survey spectrum of the Co_3Mo_3N/Co_4N/Co heterostructure compared to Co_4N/Co. In Figure 3a, the high-resolution Co 2p spectrum for Co_4N/Co exhibits two peaks at binding energies of 779.7 eV and 794.8 eV, which were attributed to the metallic Co. In addition, the prominent peaks at 781 eV and 796.5 eV and the tiny peaks at 787.4 eV and 803.5 eV were ascribed to the Co–N bond and satellite peaks, respectively.[24] It is well known that Co_3Mo_3N is composed of Co_8 clusters and Mo_3N, meaning that there are no Co–N bonds within its composition.[25] However, compared with Co_4N/Co, the Co–N peak of Co_3Mo_3N/Co_4N/Co shifts to a higher binding energy, suggesting that the introduction of Co_3Mo_3N can lead to an electron redistribution at the Co_3Mo_3N/Co_4N interface. Moreover, the high-resolution N 1s spectra show two peaks located at 398.5 and 396 eV, corresponding to Co–N and N–H bonds in Co_4N/Co (Figure 3b).[26] After introducing Co_3Mo_3N, two new peaks at 394 eV and 397.8 eV are observed, corresponding to the Mo 3p region and the Mo–N bond.[27] More importantly, the Co–N peak shifts towards a lower binding energy, which again proves that Co_3Mo_3N and Co_4N have a strong interaction. In addition, in the high-resolution Mo 3d spectrum of Co_3Mo_3N/Co_4N/Co (Figure 3c), the peaks at 228.1/231.5 eV, 229/232.4 eV, and 235.5 eV are assigned to Mo^0, $Mo^{\delta+}$, and satellite, respectively.[27] The carbon peak did not change after the introduction of Co_3Mo_3N, indicating that the carbon in the sample did not react with the metal ions (Figure S9b). In addition, the high-resolution C 1s spectrum exhibited three peaks at 284.30, 284.95, and 286.05 eV, demonstrating the presence of alternating C=C and C–C commensurate to graphene, C–O, and C=O, respectively.[28] The afore-mentioned XPS results confirm that the induced Co_3Mo_3N can lead to a redistribution of the interface charges between Co_3Mo_3N and Co_4N, which may be beneficial for HER and OER activity.

To further clarify the change of charges between Co_3Mo_3N and Co_4N in the heterostructure, ultraviolet photoemission spectroscopy (UPS) measurements were performed. As shown in Figure S10, the density of filled states of Co_3Mo_3N/Co_4N/Co and Co_4N/Co extends to the Fermi level, confirming that these materials have metallic properties.[29] Furthermore, the work function was calculated according to the equation of $W = hv - E_{cutoff}$, where hv is the incident photon energy (21.22 eV) and E_{cutoff} is the

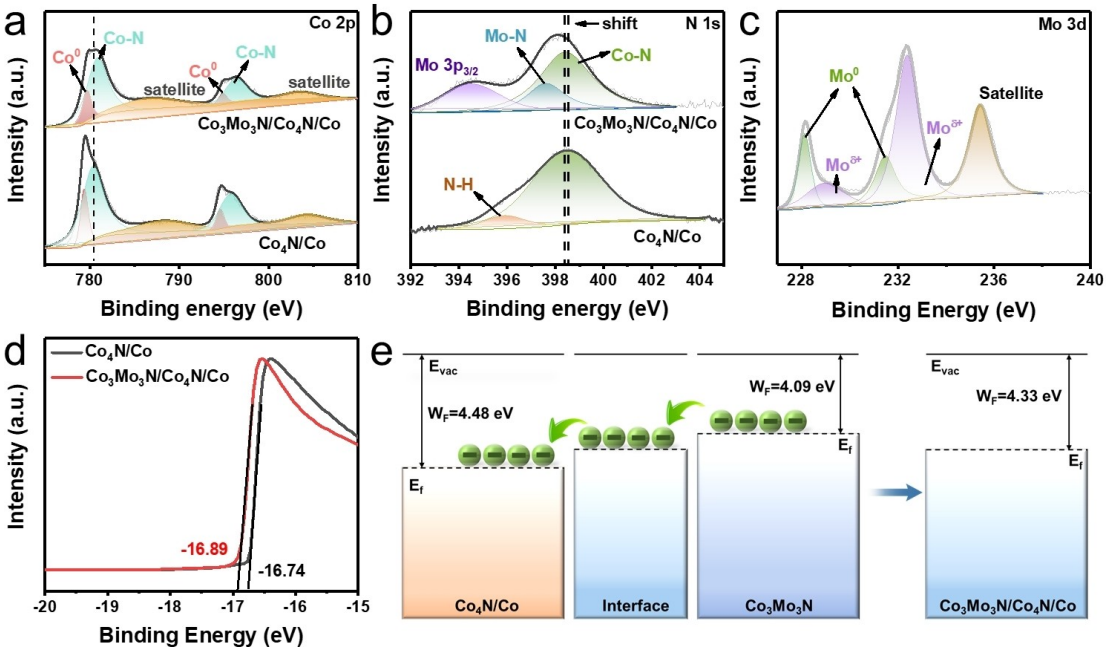

Figure 3. High-resolution XPS patterns of (a) Co 2p, (b) N 1s, and (c) Mo 3d for Co_3Mo_3N/Co_4N/Co and Co_4N/Co. (d) UPS patterns of Co_3Mo_3N/Co_4N/Co and Co_4N/Co. (e) Energy band diagrams of metallic Co_4N/Co and Co_3Mo_3N/Co_4N/Co.

normalized secondary electron cutoff (Figure 3d). Values of 4.33 and 4.48 eV were determined for $Co_3Mo_3N/Co_4N/Co$ and Co_4N/Co, respectively. In Figure S11, the work function of Co_3Mo_3N is 4.09 eV, which is calculated by density functional theory (DFT). Therefore, it is to be expected that electrons will be transferred from Co_3Mo_3N to Co_4N/Co due to the difference in work functions (Figure 3e). In addition, the Raman peak of Co_4N in the $Co_3Mo_3N/Co_4N/Co$ heterostructure shifts to lower wavenumber compared to pure Co_4N/Co, which also shows that electrons are injected into Co_4N (Figure S6a). It is reported that the Co sites in Co_4N have a too strong adsorption force for H, which is not conducive to the desorption of H_2.[9] The flow of electrons into Co_4N is beneficial to reduce the bond energy of the Co–H, thereby improving the HER efficiency.

The HER and OER performances of the various catalysts were evaluated in 1 M KOH with a standard three-electrode system. As shown in Figure 4a, $Co_3Mo_3N/Co_4N/Co$ displays small overpotentials of −78 mV for achieving current densities of $-10\ mA\ cm^{-2}$ during HER, which is close to the value of the state-of-the-art Pt/C catalyst. The HER performance of $Co_3Mo_3N/Co_4N/Co$ is better than Co_4N, Co, Co_4N/Co, Co_3Mo_3N/Co_4N and Co_3Mo_3N/Co (Figure S12 and Figure S13), meaning that the synergy of Co_3Mo_3N, Co_4N and Co can improve the HER activity. After adjusting the pyrolysis temperature of the Mo/ZIF–L precursor, $Co_3Mo_3N/Co_4N/Co$-750 shows the best HER performance. In addition, the Tafel slope of $Co_3Mo_3N/Co_4N/Co$-750 is 68 mV dec^{-1}, which is lower than that for $Co_3Mo_3N/Co_4N/Co$-700, $Co_3Mo_3N/Co_4N/Co$-800, and Co_4N/Co and comparable with commercial Pt/C, indicating the fastest reaction kinetics of $Co_3Mo_3N/Co_4N/Co$-750 toward HER (Figure 4b). The electrochemically active surface area (ECSA) is a vital component for the HER activity. The ECSAs of the catalysts were determined based on the double-layer capacitances (C_{dl}) obtained through CV measurements (Figure S14a–d). Accordingly, the double-layer capacitance (C_{dl}) of $Co_3Mo_3N/Co_4N/Co$-750 is 15.4 $mF\ cm^{-1}$, and hence, 4.05, 2.08, and 1.37 times higher than that of Co_4N/Co, $Co_3Mo_3N/Co_4N/Co$-700, and $Co_3Mo_3N/Co_4N/Co$-800, respectively (**Figure S14e**). Therefore, the corresponding ECSA of $Co_3Mo_3N/Co_4N/Co$-750 is 256 cm^2 and thus higher than for the other catalysts, revealing more exposure of active sites (Figure S14f). Notably, $Co_3Mo_3N/Co_4N/Co$

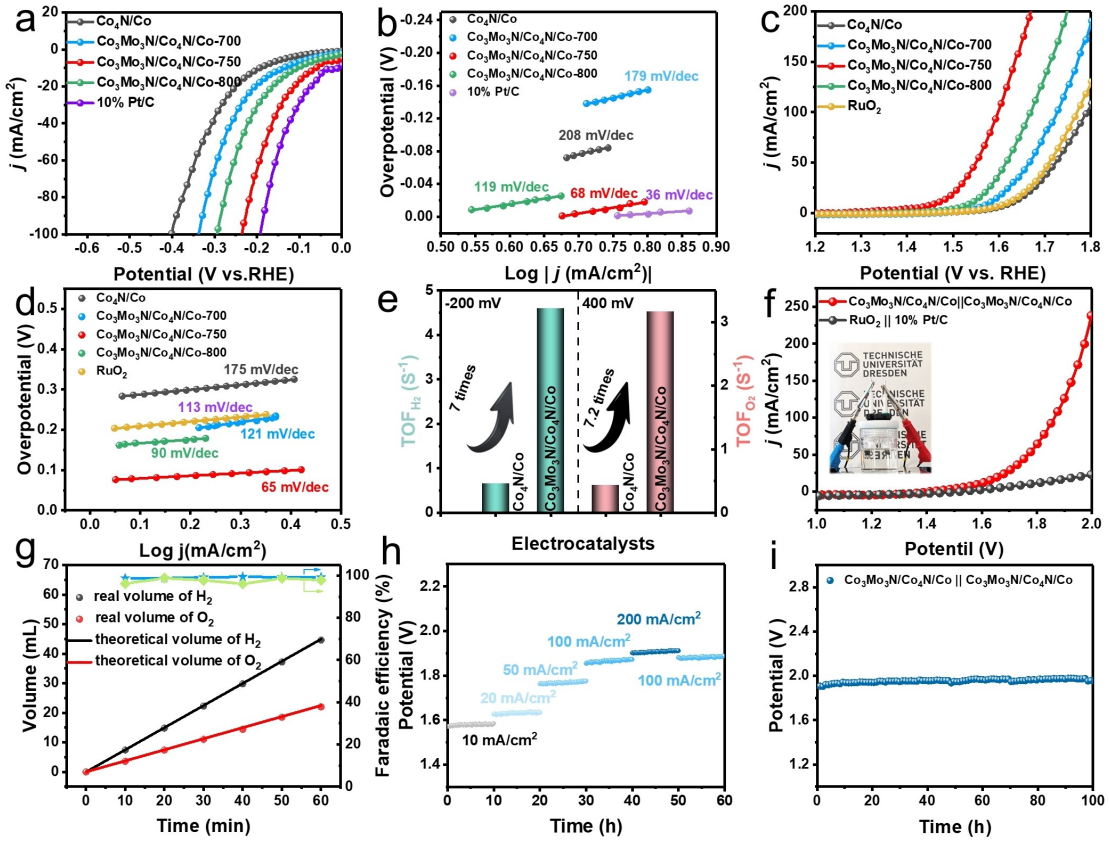

Figure 4. (a) HER polarization curves of Co_4N/Co, $Co_3Mo_3N/Co_4N/Co$ obtained at different pyrolysis temperatures, and 10% Pt/C and (b) corresponding Tafel plots. (c) OER polarization curves of Co_4N/Co, $Co_3Mo_3N/Co_4N/Co$ obtained at different pyrolysis temperatures, and RuO_2 and (d) corresponding Tafel plots. (e) TOF values of HER and OER at −200 mV and 400 mV. (f) Overall water splitting performance of $Co_3Mo_3N/Co_4N/Co||Co_3Mo_3N/Co_4N/Co$ and $RuO_2||10\%$ Pt/C with a two-electrode system. (g) Gas volume produced in the HER and OER and corresponding Faraday efficiencies. Blue and green lines represent the Faraday efficiency of H_2 and O_2, respectively. (h) Chronopotentiometry curves of $Co_3Mo_3N/Co_4N/Co||Co_3Mo_3N/Co_4N/Co$ at different current densities. (i) Chronopotentiometry curves of $Co_3Mo_3N/Co_4N/Co||Co_3Mo_3N/Co_4N/Co$ at 200 $mA\ cm^{-2}$.

still shows improved HER activities compared to Co_4N/Co, even after the current densities are ECSA-normalized (Figure S15), indicating its higher intrinsic activity. More importantly, the low overpotential of 78 mV in alkaline medium for Co_3Mo_3N/Co_4N/Co-750 outperforms most reported alkaline HER electrocatalysts (Table S1). To evaluate the structure stability of Co_3Mo_3N/Co_4N-750 during HER, SEM image and XRD analysis were conducted after a long-term stability test (Figure S16 and S17). These results show that Co_3Mo_3N/Co_4N-750 is characterized by an extremely high morphological and structural stability.

Interestingly, Co_3Mo_3N/Co_4N/Co can also exhibit superior OER performance in alkaline media. According to Figure 4c and Figure S18, Co_3Mo_3N/Co_4N/Co-750 displays a low overpotential of 220 mV at 10 mA cm^{-2}, much smaller than that of commercial RuO_2 and the other catalysts of this study. Moreover, the Tafel slope is only 65 mV dec^{-1} for Co_3Mo_3N/Co_4N/Co-750, i.e., much lower than that of commercial RuO_2 and Co_4N/Co, indicating superior reaction kinetics of Co_3Mo_3N/Co_4N/Co-750 for alkaline OER. Similar to the HER process, Co_3Mo_3N/Co_4N/Co still shows improved OER activities compared to Co_4N/Co, even after the current densities are ECSA-normalized (Figure S19), indicating their higher OER intrinsic activities. Importantly, Co_3Mo_3N/Co_4N/Co-750 shows with 220 mV one of the lowest overpotential of compared to reported alkaline OER electrocatalysts (Table S1). In order to investigate the intrinsic catalytic activity of the electrocatalysts, the turnover frequencies (TOF) of HER and OER were evaluated at different potentials (Figure 4e and Figure S20 and S21). At an overpotential of −200 mV, the HER-TOF value of Co_3Mo_3N/Co_4N/Co-750 is around 4.6 H_2 s^{-1}, which is better than that of Co_4N/Co (0.645 H_2 s^{-1}). Besides, the OER-TOF value of Co_3Mo_3N/Co_4N/Co-750 (3.16 O_2 s^{-1}) is also higher than that of Co_4N/Co (0.42 O_2 s^{-1}) at 400 mV. The above results indicate the excellent intrinsic catalytic activity of the Co_3Mo_3N/Co_4N/Co-750 electrocatalyst.

Motivated by its impressive performance, Co_3Mo_3N/Co_4N/Co-750 was utilized as both anode and cathode electrocatalyst in a two-electrode cell toward alkaline overall water splitting (Figure 4f). Commercial RuO_2 and Pt/C were used for comparison. Notably, Co_3Mo_3N/Co_4N/Co-750||Co_3Mo_3N/Co_4N/Co-750 exhibits excellent activity toward overall water splitting. In 1 M KOH, the cell potential is 1.58 V at 10 mA cm^{-2}. To achieve the same current density, a much higher cell potential is needed for commercial RuO_2||Pt/C. In order to check whether all electrons are used in both the HER and OER processes during water splitting, we collected H_2 and O_2 separately using an H-type electrolytic cell and calculated their Faraday efficiencies (Figure S22). In Figure 4g, the Faraday efficiencies of both the HER and OER process are close to 100 %, proving that there are no side reactions in the processes. Furthermore, the electrochemical durability of Co_3Mo_3N/Co_4N/Co-750||Co_3Mo_3N/Co_4N/Co-750 and commercial RuO_2||Pt/C were explored by chronopotentiometry tests at different current densities in 1 M KOH. For commercial RuO_2||Pt/C, the cell potential strongly increases after 1 h (Figure S23), which is ascribed to the unstable crystal structure of RuO_2 and also consistent with literatures.[11,30,31] In contrast, Co_3Mo_3N/Co_4N/Co-750||Co_3Mo_3N/Co_4N/Co-750 can deliver superior durability over a wide range of current densities (0–200 mA cm^{-2}) and is stable up to 100 h, even at a current density of 200 mA cm^{-2} (Figure 4h and 4i).

To gain deeper insight into the HER and OER mechanisms, operando Raman spectroscopy was utilized at different potentials. During the HER process, the in situ electrochemistry-Raman (EC-Raman) measurements were performed at the reduction potential to achieve surface structure information of Co_3Mo_3N/Co_4N/Co-750 and Co_4N/Co. It is reported that the protons of the alkaline HER originate from the water dissociation process.[32] Therefore, it is extremely important to understand the evolution of interfacial water molecules on the catalyst surface. First, in situ Raman spectroscopy testing of the support (carbon cloth) was used to rule out the influence of carbon cloth on the evolution of interfacial water (Figure S24). In Figure S24a, the two peaks located at 1350 and 1580 cm^{-1} are associated with the D and G bands of carbon.[33] After applying the potential, no new peaks appear, indicating that the carbon cloth has no effect on the adsorption of H_2O during the HER process. Because the Raman peak of H_2O overlaps with the G band of carbon, D_2O was used to perform tests for in situ Raman experiments. In Figure 5a, when the catalyst is immersed into KOH solution, the vibrational peak of D_2O increases and shifts from 1200 cm^{-1} to 1225 cm^{-1} as the reduction potential increases, indicating the formation of asymmetric H_2O adsorption on the catalyst with H-down structure. In Figure 5b, the Raman spectra of Co_3Mo_3N/Co_4N/Co-750 and Co_4N/Co show a broad peak from 3200 cm^{-1} to 3600 cm^{-1} assigned to the O–H stretching mode of interfacial water. This interfacial water peak can be described with three peaks (Figure S25 and S26). In particular, the peaks at 3225 cm^{-1}, 3450 cm^{-1}, and 3560 cm^{-1} belong to the tetrahedral, trihedral, and free water.[34] The free water has the H-down structure, indicating it is readily adsorbed on the catalyst surface. It is well known that the larger the proportion of free water, the lower the energy required for the dissociation of water, since the activation energy of free water is smaller than that of tetrahedrally and trihedrally coordinated water.[35] According to Figure 5c, for Co_3Mo_3N/Co_4N/Co-750, when the voltage was increased from −0.75 to −0.85 V, the proportion of free water (3560 cm^{-1}) also increased, indicating that it was easy to disrupt the hydrogen-bonding structure of tetra- and tricoordinated water, thus generating more free water. Compared to Co_4N/Co, the faster growth rate of free water on the surface of Co_3Mo_3N/Co_4N/Co-750 indicates a faster water adsorption rate. When the voltage was increased to −0.9 V, the water dissociation process and the free water transfer process to the catalyst surface proceeded simultaneously. Therefore, the decrease in the free water peak is due to the faster rate of hydrolysis than the adsorption of water. However, for Co_4N/Co, the free water peak starts to decrease significantly at −1 V. The free water peak decreases at a faster rate for Co_3Mo_3N/Co_4N/Co-750 than for Co_4N/Co, indicating that it decomposes water faster. Accordingly, in Figure 5d, the protons adsorbed on the

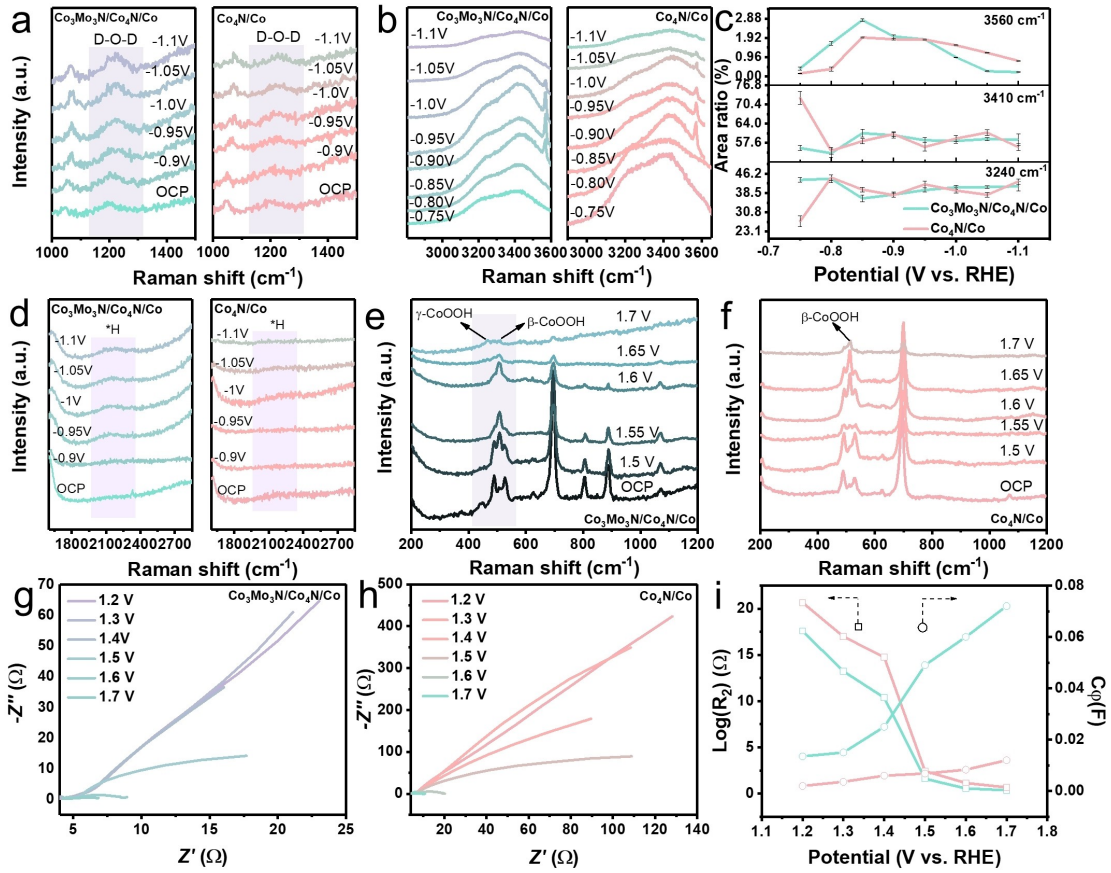

Figure 5. (a, b, d) In operando Raman spectra of $Co_3Mo_3N/Co_4N/Co$, and Co_4N/Co at different potentials during the HER. (c) Corresponding specific peak intensity of various peaks conducted from b. In operando Raman spectra of $Co_3Mo_3N/Co_4N/Co$ (e) and Co_4N/Co (f) at different potentials during the OER. Nyquist plots of $Co_3Mo_3N/Co_4N/Co$ (g) and Co_4N/Co (h) at different potentials during the OER. (i) R_2 and C_φ extracted from g and h.

$Co_3Mo_3N/Co_4N/Co$-750 surface were detected, while the adsorbed protons were not detected on the Co_4N/Co surface due to its slow hydrolysis rate. Finally, the adsorbed H on the $Co_3Mo_3N/Co_4N/Co$-750 surface will combine with another water molecule to produce H_2.

Further analysis of the improved OER performance was done using in situ EC-Raman spectroscopy. The nitrides of the transition metals tend to form a thin layer of the corresponding (hydro)oxides at anodic currents when they get in contact with strong alkaline solutions, which means these new species are likely to play a vital role in the OER.[4] In Figure 5e and **5f**, for $Co_3Mo_3N/Co_4N/Co$-750, the new phase β-CoOOH appeared when the potential was increased to 1.5 V. When the potential was increased to 1.7 V, partial conversion of β-CoOOH into γ-CoOOH was observed. For Co_4N/Co, only when the voltage was increased to 1.55 V, a weak β-CoOOH peak became visible. After the OER test, the CoOOH peak in both samples still existed, indicating the formation of an active phase on the catalyst surface (Figure S27). The XRD also proved the existence of CoOOH after the OER (Figure S28). Moreover, the Raman peak of β-CoOOH (508 cm^{-1}) in $Co_3Mo_3N/Co_4N/Co$-750 is shifted toward lower wavenumbers compared to that in Co_4N/Co (511 cm^{-1}), indicating that the β-CoOOH phase is more likely to form in $Co_3Mo_3N/Co_4N/Co$-750. Therefore, the mixed β-CoOOH and γ-CoOOH phases that are more readily formed on the $Co_3Mo_3N/Co_4N/Co$-750 surface play a crucial role to the enhancement of the OER activity.

In order to gain more information on the OER kinetics at the electrocatalyst surface, in operando Electrochemical Impedance Spectroscopy (EIS) was performed. The equivalent circuit diagram of the two processes, i.e., the electrooxidation process (high frequency 10^5–10^1 Hz) and the OER process (low frequency 10^1–10^{-1} Hz), is given in Figure S29. The solution resistance, the electrooxidation process resistance, and the OER process resistance are denoted as R_s, R_1, and R_2, respectively. The fitted Nyquist data according to the circuit diagram were plotted with increased potential from 1.2 to 1.6 V (Figure 5g and 5i). In Figure S30, R_1 for $Co_3Mo_3N/Co_4N/Co$-750 is smaller than for Co_4N/Co. This means that the introduction of Co_3Mo_3N can lower the energy barrier of cobalt oxidation, which is also consistent with the operando Raman results. Moreover, the evolution of the reactant *OH on the catalyst surface can be described by R_2. In Figure 5i, R_2 for $Co_3Mo_3N/Co_4N/Co$-750 is much lower than for Co_4N/Co in the whole potential range, revealing the faster kinetics for the adsorption of *OH. The

pseudocapacitance arising from *OH is defined as C_2, which is utilized to quantify the adsorption coverage of *OH. C_2 of $Co_3Mo_3N/Co_4N/Co$-750 is higher than that of Co_4N/Co in the whole potential range, indicating a higher *OH coverage for $Co_3Mo_3N/Co_4N/Co$-750. The rapid *OH accumulation of $Co_3Mo_3N/Co_4N/Co$-750 is expected to favor of overall catalytic driving force. Moreover, the adsorbed *OH on the electrocatalysts was evaluated based on the Laviron equation.[36] In Figure S31, the steady redox currents all exhibit a linear correlation with the square root of the scan rate in the CV. The k_s value of $Co_3Mo_3N/Co_4N/Co$-750 is 0.097 s^{-1}, which is larger than that of Co_4N/Co, revealing the strong binding force of *OH. The above results suggest that following the incorporation of Co_3Mo_3N, $Co_3Mo_3N/Co_4N/Co$ exhibits an enhanced ability to adsorb *OH, facilitating the formation of the genuine active oxide species CoOOH on its surface. Therefore, $Co_3Mo_3N/Co_4N/Co$-750 exhibits enhanced OER activity.

To further decipher the origin of $Co_3Mo_3N/Co_4N/Co$ for promoting the HER and OER performance from a theoretical perspective, density functional theory (DFT) calculations were performed. According to the XPS analysis, the introduction of Co_3Mo_3N alters the electronic structure of Co_4N, implying that the Co_3Mo_3N/Co_4N heterointerface in $Co_3Mo_3N/Co_4N/Co$-750 is critical for the HER and OER enhancement. Therefore, Co_4N, Co_3Mo_3N, and Co_3Mo_3N/Co_4N models were constructed (Figure 6a and S32). Apparently, in Figure 6b, the coupling of Co_4N and Co_3Mo_3N leads to a local charge redistribution at the interface, which is consistent with the XPS and Raman analyses. By encouraging robust interfacial charge transfer, the *d*-band center (ε_d) in the heterostructures can be adjusted effectively. The adsorption/desorption of protons as well as the water dissociation of active intermediates are both modulated by this adjustment. Therefore, the electrocatalytic performance is enhanced.

To reflect the change in ε_d, the density of states (DOS) was examined. In Figure 6c, the electronic states of the Co_3Mo_3N/Co_4N heterostructure are greater in intensity than those of Co_3Mo_3N and Co_4N at the Fermi level (E_f), indicating an enhanced conductivity. Compared to Co_3Mo_3N and Co_4N, ε_d of Co_3Mo_3N/Co_4N shows an upshift closer to the Fermi level (Figure S33). The adsorption strength of the catalysts toward H_2O reactants rises linearly with *d*-band center upshifts, in accordance with the *d*-band center theory.[37] Accordingly, Co_3Mo_3N/Co_4N has the strongest

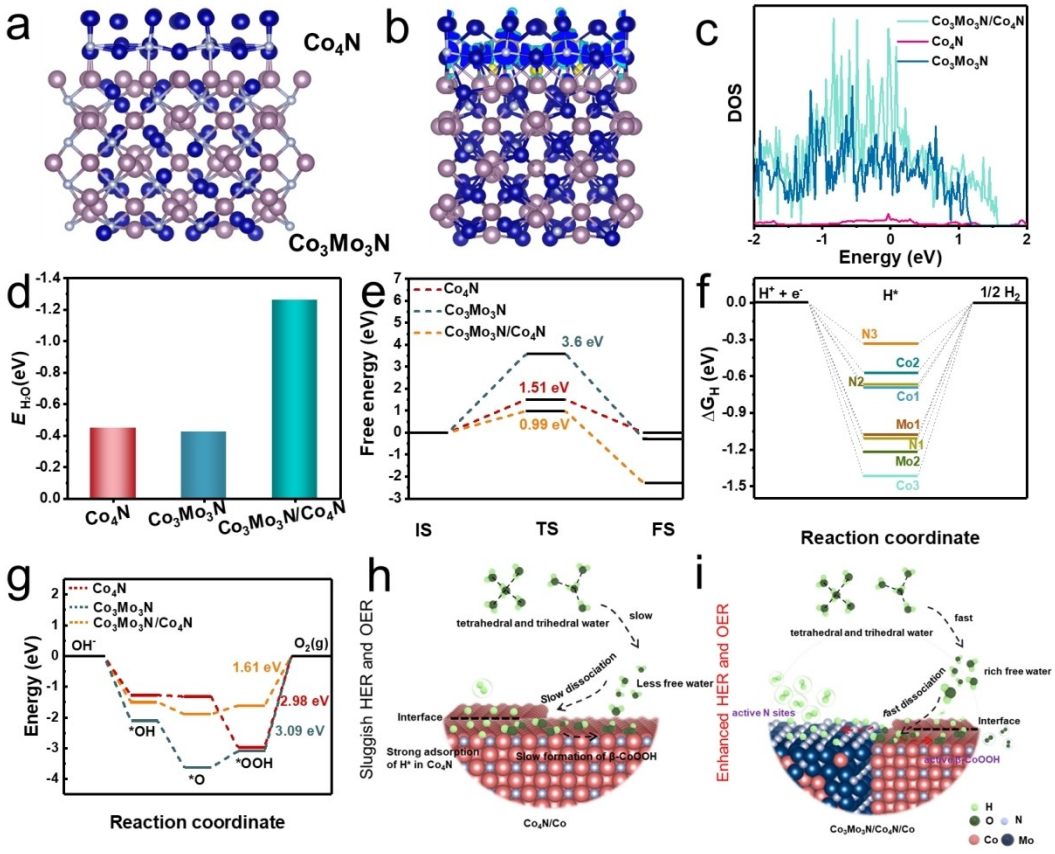

Figure 6. (a) Theoretical model of the optimized Co_3Mo_3N/Co_4N heterointerface. (b) Charge density difference plot at the Co_3Mo_3N/Co_4N heterointerface. Yellow bubbles represent electron gain and blue bubbles represent electron loss. (c) Density of states of Co_3Mo_3N, Co_4N, and Co_3Mo_3N/Co_4N. (d) Water adsorption energy of Co_3Mo_3N, Co_4N, and Co_3Mo_3N/Co_4N. (e) Water dissociation energy of Co_3Mo_3N, Co_4N, and Co_3Mo_3N/Co_4N. (f) Gibbs free energy of adsorbed H at different sites in Co_3Mo_3N, Co_4N, and Co_3Mo_3N/Co_4N. Co1, N1 are the sites in Co_4N. Mo1, Co2, and N2 are the sites in Co_3Mo_3N. Mo2, Co3, and N3 are the sites in Co_3Mo_3N/Co_4N. (g) Free energy diagram of the OER for Co_3Mo_3N, Co_4N, and Co_3Mo_3N/Co_4N. (h) The sluggish OER mechanism of Co_4N/Co. (i) The extended OER mechanism of $Co_3Mo_3N/Co_4N/Co$.

adsorption strength toward H_2O (Figure 6d). Due to the strong H_2O adsorption on the Co_3Mo_3N/Co_4N heterointerface, the H–O bond of the adsorbed H_2O can be prolonged, facilitating the dissociation of H_2O and significantly speeding up the slow Volmer step of alkaline HER. As expected, in Figure 6e, Co_3Mo_3N/Co_4N exhibits the lowest water dissociation energy (0.9 eV), compared with Co_3Mo_3N (3.6 eV) and Co_4N (1.51 eV). For the alkaline HER, after the water dissociation process, the most important step is the adsorption of protons on the catalyst surface. In Figure 6f, the Gibbs free energy (ΔG_H) of the N sites is closer to the thermoneutral value ($\Delta G_H = 0$) than for other sites in the Co_3Mo_3N/Co_4N heterostructure, meaning that the actually active sites are N sites not the Co and Mo sites. Also, ΔG_H of the N sites in the Co_3Mo_3N/Co_4N heterostructure are closer to zero than that for Co_3Mo_3N and Co_4N, suggesting the best HER performance. Then, the free energy of adsorption of oxygen intermediates was calculated based on different models to investigate the relationship between the electronic structure and OER performance. During the OER process, there are three intermediates (*OH, *O, and *OOH) formed. For the free energy diagram of Co_3Mo_3N and Co_4N, the rate determining step (RDS) is the oxidation of *OOH to O_2. After introducing Co_3Mo_3N, the RDS for $Co_3Mo_3N/Co_4N/Co$ is also the oxidation of *OOH to O_2, but with a smaller ΔG of 1.61 eV. The decrease in ΔG indicates that the optimized electronic structure of heterogeneous interfaces is essential for improving the OER performance.

Based on the above analyses, the enhanced HER and OER mechanisms of the $Co_3Mo_3N/Co_4N/Co$ heterostructure can be summarized as shown in Figure 6h and **6i**. First, the enhanced HER can be rationalized as follows. For Co_4N/Co, free water is first adsorbed at the cobalt sites to form Co-*H_2O. Further, the adsorbed water is decomposed to form Co–H and OH^-. The proton adsorbed at the Co site combines with another molecule of water and cleaves to form H_2. Although the Co sites in Co_4N have a large ΔG_H, the latter can be optimized by coupling with metallic cobalt. However, in this process, the Co site has a weak adsorption capacity for free water and requires high energy to cleave the water, resulting in a slow alkaline HER kinetics. When Co_3Mo_3N is introduced, the heterogeneous interface formed by Co_3Mo_3N and Co_4N enhances the adsorption capacity of water, while decreasing the water dissociation energy. In addition, the optimized N atoms at the heterogeneous interface have suitable adsorption and desorption capacities for H, accelerating the rate of H_2 generation. As a result, $Co_3Mo_3N/Co_4N/Co$ exhibits excellent alkaline HER properties. Then, the enhanced OER can be summarized as follows. The introduction of Co_3Mo_3N upshifts the *d*-band center of $Co_3Mo_3N/Co_4N/Co$ leading to increased adsorption of *OH. Meanwhile, the real active species β-CoOOH and γ-CoOOH are more easily formed compared to Co_4N/Co. As a result, $Co_3Mo_3N/Co_4N/Co$ exhibits excellent OER performance.

3. Conclusion

In order to accelerate the water electrolysis at high current densities, a metallic heterostructure $Co_3Mo_3N/Co_4N/Co$ was created with improved electron transfer efficiency and fast reaction dynamics. The upshift of the *d*-band center caused by the charge transfer in the $Co_3Mo_3N/Co_4N/Co$ heterostructure is advantageous for the adsorption of H_2O and *OH. On the one hand, increased H_2O adsorption on the surface of the heterostructure reduces the energy of water dissociation and accelerates proton production, hence enhancing the HER. The optimized interface electronic structure, on the other hand, makes it easier for the Co sites in the $Co_3Mo_3N/Co_4N/Co$ heterostructure to adsorb *OH species and produce the β-CoOOH and γ-CoOOH active phases, thus improving the OER performance. This work presents a new viewpoint on the construction of transition-metal-based metallic heterostructures for overall water splitting.

Acknowledgements

Y. Liu and L. Wang contributed equally to this work. The authors acknowledge Andreas Worbs for preparing the TEM lamella. Prof. Nikolai Gaponik is acknowledged for his valuable suggestions during the experiment. X. Zhang acknowledges the support from the National Natural Science Foundation of China (Grants No. 12274112). Y. Liu acknowledges the support from the China Scholarship Council (Grant No. 202106750023). Furthermore, the use of the HZDR Ion Beam Center TEM facilities and the funding of TEM Talos by the German Federal Ministry of Education and Research (BMBF, Grant No. 03SF0451) in the framework of HEMCP are acknowledged. Y. Vaynzof acknowledges the funding from the European Research Council (ERC) under the European Union's Horizon 2020 research and innovation programme (ERC Grant Agreement n° 714067, ENERGYMAPS). A. Eychmüller acknowledges support from the DFG (RTG 2767). Open Access funding enabled and organized by Projekt DEAL.

Conflict of Interest

The authors declare no conflict of interest.

Data Availability Statement

The data that support the findings of this study are available from the corresponding author upon reasonable request.

Keywords: metallic heterostructure · alkaline water splitting · interfacial water evolution · optimized active heterointerface

[1] M. J. Jang, S. H. Yang, M. G. Park, J. Jeong, M. S. Cha, S. H. Shin, K. H. Lee, Z. Bai, Z. Chen, J. Y. Lee, S. M. Choi, *ACS Energy Lett.* **2022**, *7*, 2576.
[2] J. Shan, C. Ye, S. Chen, T. Sun, Y. Jiao, L. Liu, C. Zhu, L. Song, Y. Han, M. Jaroniec, Y. Zhu, Y. Zheng, S. Z. Qiao, *J. Am. Chem. Soc.* **2021**, *143*, 5201.
[3] Y. Wang, Y. Nian, A. N. Biswas, W. Li, Y. Han, J. G. Chen, *Adv. Energy Mater.* **2021**, *11*, 1.
[4] K. Zhang, R. Zou, *Small* **2021**, *17*, 1.
[5] J. Wang, H. Yang, F. Li, L. Li, J. Wu, S. Liu, T. Cheng, Y. Xu, Q. Shao, X. Huang, *Sci. Adv.* **2022**, *8*, 1.
[6] S. L. D. Nicole, Y. Li, W. Xie, G. Wang, J. M. Lee, *Small* **2023**, *19*, 1.
[7] Z. Wang, J. Huang, L. Wang, Y. Liu, W. Liu, S. Zhao, Z. Liu, *Angew. Chem.* **2022**, *134*.
[8] Y. Yu, J. Zhou, Z. Sun, *Adv. Funct. Mater.* **2020**, *30*, 1.
[9] P. Zhou, G. Hai, G. Zhao, R. Li, X. Huang, Y. Lu, G. Wang, *Appl. Catal. B* **2023**, *325*.
[10] A. Rubab, N. Baig, M. Sher, M. Ali, A. Ul-Hamid, N. Jabeen, L. U. Khan, M. Sohail, *ChemNanoMat* **2022**, *8*.
[11] Y. Li, Q. Zhang, X. Zhao, H. Wu, X. Wang, Y. Zeng, Q. Chen, M. Chen, P. Liu, *Adv. Funct. Mater.* **2023**, *33*.
[12] H. Ma, Z. Chen, Z. Wang, C. V. Singh, Q. Jiang, *Adv. Sci.* **2022**, *9*, 1.
[13] N. Yao, Z. Fan, Z. Xia, F. Wu, P. Zhao, G. Cheng, W. Luo, *J. Mater. Chem. A* **2021**, *9*, 18208.
[14] M. Qin, L. Chen, H. Zhang, M. Humayun, Y. Fu, X. Xu, X. Xue, C. Wang, *Chem. Eng. J.* **2023**, *454*, 140230.
[15] S. Zhang, L. Wang, T. Xie, Q. Chen, W. Peng, Y. Li, F. Zhang, X. Fan, *J. Mater. Chem. A* **2022**, *10*, 21523.
[16] A. Mahmood, S. Khan, F. Rahayu, A. U. H. A. Shah, A. U. Rahman, T. Muhammad, A. Khan, N. Ullah, *Energy Technol.* **2023**, *11*, 1.
[17] Y. Yuan, S. Adimi, T. Thomas, J. Wang, H. Guo, J. Chen, J. P. Attfield, F. J. DiSalvo, M. Yang, *Innovation* **2021**, *2*.
[18] Y. Bian, S. Wang, D. Jin, R. Wang, C. Chen, L. Zhang, *Nano Energy* **2020**, *75*, 104935.
[19] X. Wang, X. Han, R. Du, C. Xing, X. Qi, Z. Liang, P. Guardia, J. Arbiol, A. Cabot, J. Li, *ACS Appl. Mater. Interfaces* **2022**, *14*, 41924.
[20] X. F. Lu, L. Yu, J. Zhang, X. W. (David) Lou, *Adv. Mater.* **2019**, *31*, 1.
[21] Y. Liu, H. Zhang, W. Song, Y. Zhang, Z. Hou, G. Zhou, Z. Zhang, J. Liu, *Chem. Eng. J.* **2023**, *451*, 138905.
[22] T. Zhou, J. Shen, Z. Wang, J. Liu, R. Hu, L. Ouyang, Y. Feng, H. Liu, Y. Yu, M. Zhu, *Adv. Funct. Mater.* **2020**, *30*, 1.
[23] K. Feng, J. Tian, J. Zhang, Z. Li, Y. Chen, K. H. Luo, B. Yang, B. Yan, *ACS Catal.* **2022**, *12*, 4696.
[24] K. R. Yoon, K. Shin, J. Park, S. H. Cho, C. Kim, J. W. Jung, J. Y. Cheong, H. R. Byon, H. M. Lee, I. D. Kim, *ACS Nano* **2018**, *12*, 128.
[25] C. D. Zeinalipour-Yazdi, J. S. J. Hargreaves, C. R. A. Catlow, *J. Phys. Chem. C* **2015**, *119*, 28368.
[26] H. Zhang, D. Tian, Z. Zhao, X. Liu, Y. N. Hou, Y. Tang, J. Liang, Z. Zhang, X. Wang, J. Qiu, *Energy Storage Mater.* **2019**, *21*, 210.
[27] R. Tong, M. Xu, H. Huang, J. Wu, Y. Xiong, M. Shao, Y. Zhao, S. Wang, H. Pan, *Int. J. Hydrogen Energy* **2022**, *47*, 11447.
[28] N. Ullah, M. Xie, S. Hussain, W. Yaseen, S. A. Shah, B. A. Yusuf, C. J. Oluigbo, H. U. Rasheed, Y. Xu, J. Xie, *Front. Mater.* **2021**, *15*, 305.
[29] T. Wu, S. Xu, Z. Zhang, M. Luo, R. Wang, Y. Tang, J. Wang, F. Huang, *Adv. Sci.* **2022**, *9*, 1.
[30] W. Zhai, Y. Chen, Y. Liu, T. Sakthivel, Y. Ma, S. Guo, Y. Qu, Z. Dai, *Adv. Funct. Mater.* **2023**, *33*, 1.
[31] K. Du, L. Zhang, J. Shan, J. Guo, J. Mao, C. C. Yang, C. H. Wang, Z. Hu, T. Ling, *Nat. Commun.* **2022**, *13*, 1.
[32] Q. Dai, L. Wang, K. Wang, X. Sang, Z. Li, B. Yang, J. Chen, L. Lei, L. Dai, Y. Hou, *Adv. Funct. Mater.* **2022**, *32*.
[33] X. Lin, J. Liu, X. Qiu, B. Liu, X. Wang, L. Chen, Y. Qin, *Angew. Chem. Int. Ed.* **2023**.
[34] M. Wang, K. Sun, W. Mi, C. Feng, Z. Guan, Y. Liu, Y. Pan, *ACS Catal.* **2022**, 10771.
[35] L. fan Shen, B. an Lu, Y. yang Li, J. Liu, Z. chao Huang-fu, H. Peng, J. yu Ye, X. ming Qu, J. ming Zhang, G. Li, W. bin Cai, Y. xia Jiang, S. gang Sun, *Angew. Chem. Int. Ed.* **2020**, *59*, 22397.
[36] P. Zhai, C. Wang, Y. Zhao, Y. Zhang, J. Gao, L. Sun, J. Hou, *Nat. Commun.* **2023**, *14*, 1.
[37] Q. Hu, K. Gao, X. Wang, H. Zheng, J. Cao, L. Mi, Q. Huo, H. Yang, J. Liu, C. He, *Nat. Commun.* **2022**, *13*, 1.

Manuscript received: December 13, 2023
Accepted manuscript online: February 5, 2024
Version of record online: February 22, 2024